



Molecular Investigation of Chicken Acid-Sensing Ion Channel 1 β 11-12 Linker Isomerization and Channel Kinetics

OPEN ACCESS

Edited by:

Haruyuki Kamiya,
Hokkaido University, Japan

Reviewed by:

Lachlan Rash,
The University of Queensland,
Australia
Andreas Reiner,
Ruhr University Bochum, Germany

*Correspondence:

Maria Musgaard
mariamusgaard@gmail.com
David M. MacLean
david_maclean@urmc.rochester.edu

† These authors have contributed
equally to this work

* Present address:

Maria Musgaard,
OMass Therapeutics, Oxford,
United Kingdom

Specialty section:

This article was submitted to
Cellular Neurophysiology,
a section of the journal
Frontiers in Cellular Neuroscience

Received: 20 August 2021

Accepted: 05 November 2021

Published: 24 November 2021

Citation:

Rook ML, Ananchenko A,
Musgaard M and MacLean DM
(2021) Molecular Investigation
of Chicken Acid-Sensing Ion Channel
1 β 11-12 Linker Isomerization
and Channel Kinetics.
Front. Cell. Neurosci. 15:761813.
doi: 10.3389/fncel.2021.761813

Matthew L. Rook^{1†}, Anna Ananchenko^{2†}, Maria Musgaard^{2**} and David M. MacLean^{3*}

¹ Graduate Program in Cellular and Molecular Pharmacology and Physiology, University of Rochester Medical Center, Rochester, NY, United States, ² Department of Chemistry and Biomolecular Sciences, University of Ottawa, Ottawa, ON, Canada, ³ Department of Pharmacology and Physiology, University of Rochester Medical Center, Rochester, NY, United States

Structures of the trimeric acid-sensing ion channel have been solved in the resting, toxin-bound open and desensitized states. Within the extracellular domain, there is little difference between the toxin-bound open state and the desensitized state. The main exception is that a loop connecting the 11th and 12th β -strand, just two amino acid residues long, undergoes a significant and functionally critical re-orientation or flipping between the open and desensitized conformations. Here we investigate how specific interactions within the surrounding area influence linker stability in the “flipped” desensitized state using all-atom molecular dynamics simulations. An inherent challenge is bringing the relatively slow channel desensitization and recovery processes (in the milliseconds to seconds) within the time window of all-atom simulations (hundreds of nanoseconds). To accelerate channel behavior, we first identified the channel mutations at either the Leu414 or Asn415 position with the fastest recovery kinetics followed by molecular dynamics simulations of these mutants in a deprotonated state, accelerating recovery. By mutating one residue in the loop and examining the evolution of interactions in the neighbor, we identified a novel electrostatic interaction and validated prior important interactions. Subsequent functional analysis corroborates these findings, shedding light on the molecular factors controlling proton-mediated transitions between functional states of the channel. Together, these data suggest that the flipped loop in the desensitized state is stabilized by interactions from surrounding regions keeping both L414 and N415 in place. Interestingly, very few mutations in the loop allow for equivalent channel kinetics and desensitized state stability. The high degree of sequence conservation in this region therefore indicates that the stability of the ASIC desensitized state is under strong selective pressure and underlines the physiological importance of desensitization.

Keywords: gating, desensitization, acid-sensing ion channels, ASICs, molecular dynamics

INTRODUCTION

The majority of ligand-gated ion channels (LGICs) undergo a process of desensitization wherein channels enter a long-lived non-conducting state in the continued presence of agonist (Katz and Thesleff, 1957). Thus, desensitization shapes the time course of ion flux and may also play a protective role when ligand clearance is compromised (Jones and Westbrook, 1996; Christie et al., 2010). Desensitized channels must ultimately recover from this non-conducting state before they can be activated again, and, like desensitization, the recovery time course also influences the physiological roles of LGICs (Chen et al., 2018). The era of structural biology has provided many insights and hypotheses regarding the molecular basis of desensitization for numerous LGICs (Plested, 2016; Noviello et al., 2021; Yu et al., 2021) including acid-sensing ion channels (ASICs) (Gonzales et al., 2009; Bacongus and Gouaux, 2012; Bacongus et al., 2014; Yoder et al., 2018; Yoder and Gouaux, 2020).

Acid-sensing ion channels are trimeric sodium-selective channels found throughout the brain and body (Boscardin et al., 2016). In response to a rapid drop in extracellular pH, ASICs activate and subsequently desensitize nearly completely with time constants ranging from 100 ms to 2 s, depending on the species, subunit and pH stimulus (Grunder and Pusch, 2015; Rook et al., 2021b). Recent structures of the resting, toxin-stabilized open and desensitized states of chicken ASIC1 (cASIC1) showed that the main difference in the ASIC extracellular domains of desensitized channels, relative to resting and open channels, is the isomerization of two amino acid residues linking the 11th and 12th β -strands (Yoder et al., 2018; Rook et al., 2021b). In the resting and toxin-stabilized open state, the first amino acid in this linker (Leu414) points up and away from the middle of the channel while the second amino acid (Asn415) points downward (Figures 1A,B). In the desensitized structures, this linker has isomerized or flipped such that Leu414 now points inward and Asn415 outward (Figure 1B). This was hypothesized to reflect a “molecular clutch” (Yoder et al., 2018). When the clutch is engaged, conformational changes in the extracellular domain can propagate to the pore and drive activation. However, once the clutch disengages (i.e., the linker flips), conformational changes are no longer effectively coupled to the pore. This enables the extracellular domain to remain in an “active” state while the pore can close, preventing continued ion influx under acidic conditions (Yoder et al., 2018). This elegant mechanism explains earlier functional data and was recently supported by additional mutations, simulations and state-dependent crosslinking (Rook et al., 2020). The goal of the present work was to further probe the molecular determinants of linker flipping using molecular dynamics simulations in conjunction with fast-perfusion electrophysiology.

To do this, we measured the kinetics of desensitization and recovery for a panel of mutations at both the Leu414 and Asn415 positions. We reasoned that the fastest mutations would have an increased propensity for motion of the β 11-12 linker, thus potentially allowing us to observe linker dynamics within the timeframe of MD. Thus, the fastest mutants were used for subsequent all-atom molecular dynamics simulations

to study the behavior of the β 11-12 linker. Our simulations identified previously characterized electrostatic interactions as well as a novel hydrogen bond interaction that controls the stability of the ASIC desensitized state. Taken together, these data deepen our understanding of the molecular determinants of ASIC desensitization while advancing new metrics for the analysis of these transitions.

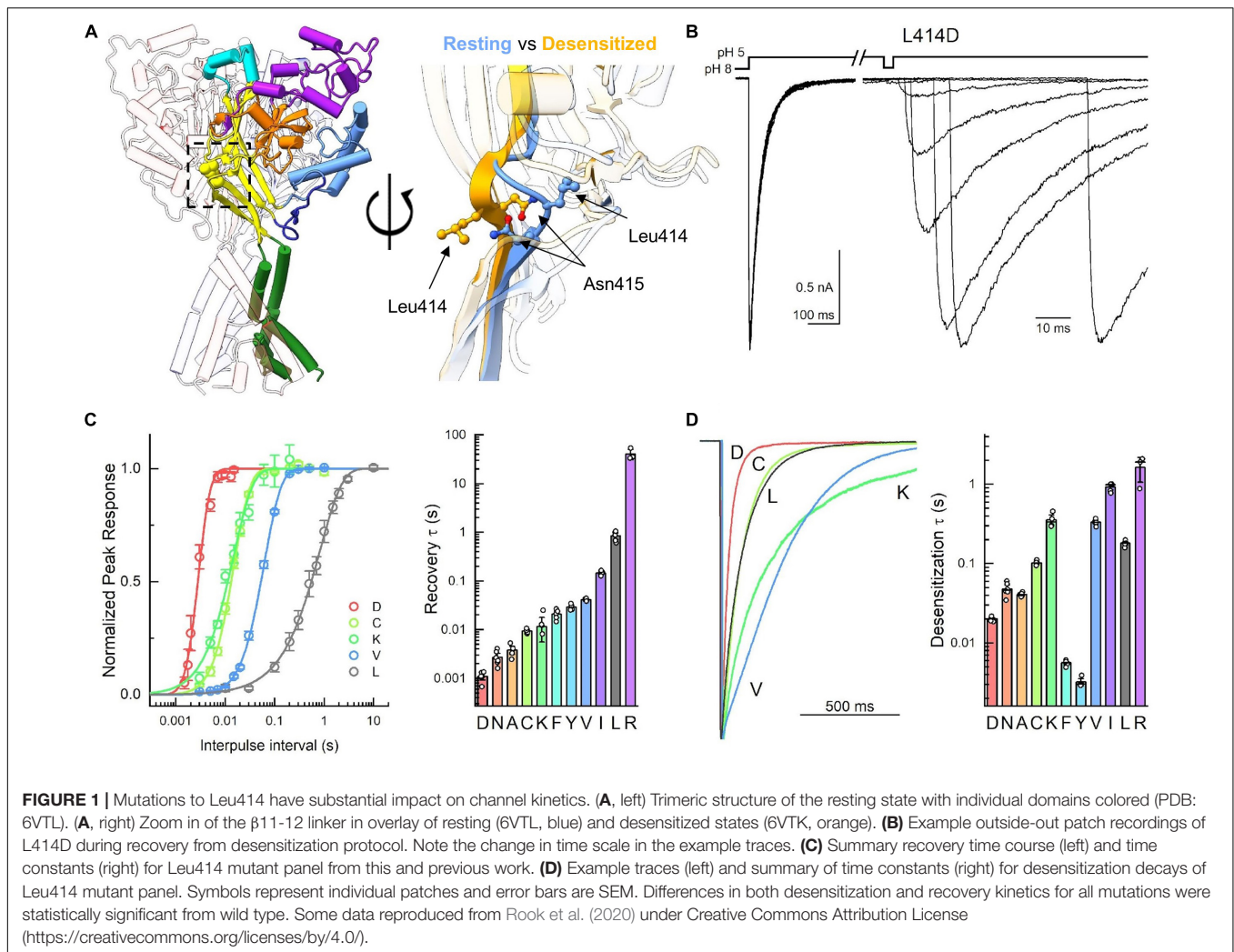
MATERIALS AND METHODS

Cell Culture, Mutagenesis and Transfection

Human Embryonic Kidney 293 ASIC1 knockout (KO) cells (Rook et al., 2021a) were maintained in Dulbecco's Modification of Eagle's Medium (DMEM) with 4.5 g/L glucose, L-glutamine and sodium pyruvate (Corning/Mediatech, Inc.) or Minimum Essential Medium (MEM) with Glutamax and Earle's Salts (Gibco), supplemented with 10% FBS (Atlas Biologicals) and penicillin/streptomycin (Invitrogen). Cells were passaged every 2–3 days when approximately 90% confluence was achieved. Cells were plated on tissue culture treated 35 mm dishes, transfected 24–48 h later and recorded from 24 to 48 h post-transfection. Cells were transiently transfected with wild type or mutations of full length cASIC1 (in pcDNA3.1(+)) along with eGFP using an ASIC:eGFP ratio of 2.5:1 μ g of cDNA per 10 mL of media. Transfections were performed using polyethylenimine 25k (PEI 25k, Polysciences, Inc.) following manufacturer's instructions, with media change at 6–8 h. Mutations were introduced using site-directed mutagenesis PCR and confirmed by sequencing (Fisher Scientific/Eurofins Genomics).

Electrophysiology and Fast Perfusion

Culture dishes were visualized using a 20 \times objective mounted on a Nikon Ti2 microscope with phase contrast. A 470 nm LED (Thorlabs) and dichroic filter cube were used to excite GFP and detect transfected HEK cells. Outside-out patches were excised using heat-polished, thick-walled borosilicate glass pipettes of 3–8 M Ω resistance. The pipette internal solution contained (in mM) 135 CsF, 33 CsOH, 11 EGTA, 10 HEPES, 2 MgCl₂, and 1 CaCl₂ (pH 7.4). External solutions with a pH greater than 7 were composed of (in mM) 150 NaCl, 20 HEPES, 1 CaCl₂, and 1 MgCl₂ with pH values adjusted to their respective values using NaOH. For solutions with a pH lower than 7, HEPES was replaced with MES at the same concentration (20 mM). All recordings were performed at room temperature with a holding potential of –60 mV using an Axopatch 200B amplifier (Molecular Devices). Data were acquired using AxoGraph software (AxoGraph) at 20 kHz, filtered at 10 kHz and digitized using a USB-6343 DAQ (National Instruments). Series resistance was routinely compensated by 90–95% where the peak amplitude exceeded 100 pA. Rapid perfusion was performed using home-built, triple-barrel application pipettes (Vitrocom), manufactured following an established protocol (MacLean, 2015). Translation of application pipettes was achieved using a piezo translator (P601.40 or P212.80, PI) mounted to a manual manipulator and driven by a voltage power supply (E505.00 or E-471.20, PI).



Voltage commands to the piezo were first low-pass filtered (eight-pole Bessel; Frequency Devices) at 50–100 Hz. Solution exchange was routinely measured at the end of each patch recording using open tip currents with exchange times ranging from 250 to 500 μ s.

Molecular Dynamics Simulations

Molecular dynamics simulations were performed using a cASIC1 structure solved at 3 Å resolution in a proposed desensitized state (PDB ID: 4NYK) (Gonzales et al., 2009). In this crystal structure, residues 42–455 were resolved, of which 23 residues had missing atoms, which were modeled using MODELLER 9v20 (Sali and Blundell, 1993). Missing residues at the N- and C-termini were disregarded. Bound chloride ions and crystallographically resolved water molecules were retained. The orientation of the structure for placement in the lipid bilayer was obtained from the Orientations of Proteins in Membranes (OPM) database (Lomize et al., 2012). Disulfide bonds for each chain were maintained between the following cysteine pairs: C94-C195, C173-C180, C291-C366, C309-C362, C313-C360, C322-C344, and C324-C336. All residues were kept in their standard ionization state.

To construct the simulation system, the protein was embedded in a 120×120 Å POPC bilayer using the CHARMM-GUI membrane builder (Jo et al., 2008), with a box length of 147 Å. The system was solvated with TIP3P water molecules and a NaCl concentration of 150 mM.

The L414D and N415G mutant systems were constructed in the same way, with mutations selected in the CHARMM-GUI interface.

The simulations were performed using GROMACS 2019.4 (Abraham et al., 2015) and the CHARMM36m forcefield was applied (Huang and MacKerell, 2013). All system constructs were minimized for 5000 steps or until a maximum force of $1000 \text{ kJ mol}^{-1} \text{ nm}^{-1}$ on any atom was reached. As per the default CHARMM-GUI method, the systems were then equilibrated in six steps. The first three steps were 125 ps long with a timestep of 1 fs. The final three steps were 500 ps long with a timestep of 2 fs. Following the default CHARMM-GUI equilibration, position restraints were gradually lifted with each equilibration step. The final production run had a timestep of 2 fs and was performed for 5×500 ns for each system, with the starting velocities of each repeat randomized prior to equilibration. Periodic boundary

conditions were applied and all systems were simulated in the NPT ensemble. The Verlet cut-off scheme was used throughout all steps with a force-switch modifier starting at 10 Å and a cut-off of 12 Å. The particle mesh Ewald (PME) method (Darden et al., 1993; Essmann et al., 1995) was used for long-range electrostatics and a cut-off of 12 Å was used for short-range electrostatics. For the equilibration steps, a temperature of 310 K was maintained using the Berendsen thermostat (Berendsen et al., 1984). The Berendsen barostat (Berendsen et al., 1984) was used to maintain a pressure of one bar for the last four steps of equilibration using semi-isotropic pressure coupling. For the production run, the Nose-Hoover thermostat (Nose, 1984; Hoover, 1985) was used to maintain temperature at 310 K and the Parrinello-Rahman barostat (Parrinello and Rahman, 1981) was used to maintain pressure at one bar using semi-isotropic pressure coupling. Covalent bonds including hydrogen atoms were constrained using the LINCS algorithm (Hess, 2008).

Analysis was performed using MDAnalysis tools (Michaud-Agrawal et al., 2011; Gowers et al., 2016) as well as in-house scripts. Structural figures prepared using VMD (Humphrey et al., 1996) and Chimera (Pettersen et al., 2004).

Sequence Alignments

Amino acid sequences for ASICs from evolutionarily distant organisms (Lynagh et al., 2018) were obtained directly from Dr. Lynagh. Sequences for mammalian, avian, amphibian and fish were obtained from NCBI. Sequences were aligned using Muscle (Edgar, 2004) with default settings. The percent conservation, logo plot and consensus sequence was calculated using Jalview (Waterhouse et al., 2009) and illustrated using Chimera (Meng et al., 2006).

Statistics and Data Analysis

Current desensitization decays were fitted using exponential decay functions in Clampfit (Molecular Devices). For recovery from desensitization experiments, the piezo command voltage was split and re-directed as an input signal. The resulting piezo “mirror” signal was used to define conditioning and test pulse epochs. A custom script in Matlab (Mathworks) was used to detect peaks within each epoch and normalize the test pulse peak to the conditioning pulse. OriginLab (OriginLab Corp.) was used to fit the normalized responses to:

$$I_t = \left(1 - e^{\left(\frac{-t}{\tau}\right)}\right)^m \quad (1)$$

where I_t is the fraction of the test peak at an interpulse interval of t compared to the conditioning peak, τ is the time constant of recovery and m is the slope of the recovery curve. Each protocol was performed between 1 and 3 times on a single patch, with the resulting test peak/conditioning peak ratios averaged together. For steady-state desensitization (SSD) curves, peak currents within a patch were normalized to the peak response evoked by pH 5.5 and fit to:

$$I_x = \frac{1}{1 + 10^{((pH_{50} - pH_x)n_H)}} \quad (2)$$

where I_x is the current obtained using a given conditioning pH value X , pH_{50} is the pH yielding half maximal response and n_H is the Hill slope. For recovery experiments and SSD, patches were individually fit and averages for the fits were reported in the text. For all experiments, N was taken to be a single patch and error is reported as SEM. Unless otherwise state, non-parametric two-tailed, unpaired randomization tests with 100,000 iterations were implemented in Python to assess statistical significance. Bonferroni-Holm corrections for multiple comparisons were used and the adjusted P -values are reported in either text, figure legend or **Table 1**. Statistical comparisons of recovery from desensitization and SSD were based on differences in recovery time constant and pH_{50} , respectively.

To assess statistical differences in side chain angles from molecular dynamics simulations, we measured the median side chain angle from all three chains within each simulation as median is less sensitive to outliers (or multiple populations) than mean. To compare side chains angles between conditions (e.g., N415 angles for wild type vs. L414D), we compared the median side chain angles for each simulation in each group using a Mann-Whitney U test where n is the number of simulations.

RESULTS

Kinetics of Desensitization and Recovery Are Strongly Influenced by Mutations to the β 11-12 Linker

With the exception of the acidic pocket, the most salient difference between the resting and desensitized states of cASIC1 is the isomerization of the linker connecting the 11th and 12th beta strands. This is illustrated in **Figure 1A** where the side chains of the linker residues are shown within the palm domain as well as superimposed in the resting and desensitized states [PDB: 6VTL and 6VTK (Yoder and Gouaux, 2020)]. In the resting state, Leu414 points outward from the central axis of the channel and slightly up. However, in the desensitized state, the Leu414 side chain swings inward and down, toward a hydrophobic cleft (Rook et al., 2020). In parallel, Asn415 rotates from a down and inward position in the resting state to an upward and out position in the desensitized state. This swivel was proposed to act as a molecular clutch, uncoupling the proton sensing extracellular domain from the channel pore and thereby allowing the extracellular domain to adopt an “active-like” protonated conformation while the pore shuts closed (Yoder et al., 2018). Consistent with this, using non-canonical amino acid trapping, we recently demonstrated that local motion of this area is critical for desensitization to occur (Rook et al., 2020). We also found that slight mutations to the Leu414 position (i.e., L414A) result in dramatic changes in channel desensitization and recovery (Rook et al., 2020). The goal of the present study was to further probe the molecular determinants of this linker isomerization using molecular dynamics simulations.

A challenge in using molecular dynamics simulations to explore functional transitions of ion channels is the discrepant time scales of molecular dynamics simulations ($\sim 10^{-7}$ s) vs. patch clamp experiments ($\sim 10^{-3}$ s). In this case, the

TABLE 1 | Time constants of desensitization and recovery.

Mutation	τ_{des} (ms)	$\tau_{des,fast}$ (ms) [% area]	$\tau_{des,slow}$ (ms) [% area]	Adj. <i>P</i> -value vs. wt	τ_{rec} (ms)	m_{rec}	Adj. <i>P</i> -value vs. wt	<i>n</i>
WT	180 ± 6	–	–		840 ± 90	0.96 ± 0.05	–	5
A83G	31 ± 2	–	–	0.00025	210 ± 30	1.2 ± 0.05	0.00014	5
L414C	100 ± 3	–	–	0.01773	9.6 ± 0.5	2.5 ± 0.2	0.0008	5
L414D	20 ± 0.6	–	–	0.00618	1.1 ± 0.1	9.7 ± 1.7	0.001	5
L414K	370 ± 60*	120 ± 32 [45 ± 5]	590 ± 140 [55 ± 5]	0.0234	21 ± 2	3.5 ± 0.5	0.0022	4
L414V	330 ± 10	–	–	0.0009	41 ± 1	2.09 ± 0.07	0.00125	5
L414N	47 ± 4	–	–	0.0126	2.7 ± 0.4	12 ± 4	0.0009	6
L414A	41 ± 1	–	–	0.01228	3.8 ± 0.5	9 ± 3	0.00087	5
L414F	56 ± 2	–	–	0.0236	21 ± 2	3.5 ± 0.5	0.00112	5
L414Y	32 ± 2	–	–	0.02805	29 ± 2	2.7 ± 0.2	0.00076	4
L414I	920 ± 50	–	–	0.00408	145 ± 6	1.40 ± 0.04	0.00108	5
L414R	1600 ± 400	–	–	0.001	40000 ± 6000	0.30 ± 0.03	0.0007	3
N415A	38 ± 2	–	–	0.0082	13 ± 1	1.9 ± 0.2	0.0014	5
N415D	110 ± 5	–	–	0.00522	46 ± 1	1.6 ± 0.04	0.00098	5
N415E	2000 ± 70	–	–	0.0012	3.2 ± 0.07	3.6 ± 0.2	0.00096	4
N415F	1500 ± 50	–	–	0.0011	22 ± 2	2.1 ± 0.3	0.0008	4
N415G	3.6 ± 0.4	–	–	0.00984	5.9 ± 0.4	1.9 ± 0.2	0.00154	5
N415I	18000 ± 400*	3000 ± 800 [42 ± 5]	30000 ± 2000 [58 ± 5]	0.00605	290000 ± 80000	0.3 ± 0.6	0.0012	3
N415K	9900 ± 600	–	–	0.00938	35 ± 4	2.8 ± 0.2	0.00032	4
N415L	7800 ± 600	–	–	0.001	860 ± 90	0.99 ± 0.05	0.85608	2
N415Q	1900 ± 100	–	–	0.00736	29 ± 5	2.2 ± 0.2	0.00048	4
N415R	4700 ± 400	–	–	0.00594	18 ± 0.5	3.3 ± 0.1	0.00126	5
N415S	53 ± 3	–	–	0.00744	45 ± 6	1.4 ± 0.04	0.00112	5
N415W	3400 ± 70	–	–	0.00848	25 ± 0.6	1.1 ± 0.1	0.00064	4

*Indicates weighted time constant.

Desensitization decays measured in pH 5. Recovery measured in pH 8.

functional transitions of interest are desensitization and recovery, respectively. To partially bridge the timescale gap, we have previously taken advantage of the pH-dependence of recovery from desensitization (Rook et al., 2020). ASICs recover faster from desensitization when incubated in more alkaline solutions. This effect is quite strong in cASIC1, which recovers with a time constant of 840 ± 90 ms at pH 8 but accelerates to 7.5 ± 0.4 ms at pH 10 (Rook et al., 2020). By starting simulations from the desensitized/protonated crystal structure and de-protonating acidic residues (i.e., approximating a functional transition from extracellular pH 5 to 9), we can provoke the beginning of the transition from desensitized to resting state. When this strategy is combined with mutations which accelerate recovery from desensitization, we have previously been able to observe the linker flipping behavior directly in molecular dynamics simulations (Rook et al., 2020). Hence, we again focused on capturing the recovery process in the simulations, rather than the desensitization process.

A second challenge or caveat in comparing molecular dynamics simulations with results from patch clamp experiments is that the measured macroscopic channel desensitization and recovery processes reflect a population of channels transitioning between resting, active, pre-active and desensitized states. Changes to one or more of these transitions may alter the macroscopic desensitization decays measured in the population

without much influence on the microscopic desensitization transition itself (Jones and Westbrook, 1996; Daniels et al., 2013). Since molecular dynamics simulations more likely reflects the single channel state transitions, we must bear this caveat in mind.

We set out to extend our previous work by first characterizing a wide range of mutations at both the Leu414 and Asn415 positions. The fastest mutations uncovered would then be used for molecular dynamics simulations to better probe the interactions governing linker isomerization. As an added benefit, these experiments would further map the structure-function relationships in this critical region.

To do this, we made four additional mutations to Leu414 in cASIC1 (D, C, K, and V). This isoform was used to enable direct comparison with past work, due to the larger number of structures and because, in our hands, cASIC1 undergoes far less tachyphylaxis [long-lived inactivation or run-down (Chen and Grunder, 2007)], thus enabling longer recordings of recovery from desensitization. To measure recovery, we excised patches from transfected ASIC KO HEK cells (Rook et al., 2021a) and used piezo-driven fast perfusion to jump from pH 8 to 5. Recovery was mapped using a standard two-pulse protocol where channels were first exposed to a conditioning pulse of pH 5 to populate the desensitized state followed by jumping to pH 8 for variable intervals before a test pulse of pH 5 is applied. Conditioning pulse durations were chosen for each mutation

to achieve equilibrium desensitization. However, the test pulse was generally 500 ms in duration (although 50 ms was used for N415G). Strikingly, each mutation showed a statistically significant difference in recovery from desensitization compared to wild type (**Figure 1C** and **Table 1**). To our surprise, we found the L414D showed the fastest recovery from desensitization ($\tau = 1.1 \pm 0.1$ ms, $m = 9.7 \pm 1.7$, $n = 5$) while the structurally smaller L414A and L414C were actually slower than L414D (**Figures 1B,C**). Even with this new expanded series, we could discern no clear pattern or structural feature that predicted fast recovery. The large and positively charged Arg side chain desensitized and recovered slowly (Rook et al., 2020), however, the smaller Lys side chain actually recovered faster than wild-type ($\tau = 21 \pm 2$ ms, $m = 3.5 \pm 0.5$, $n = 4$). Moreover, the sizeable hydrophobic side chains of Tyr and Phe recovered faster.

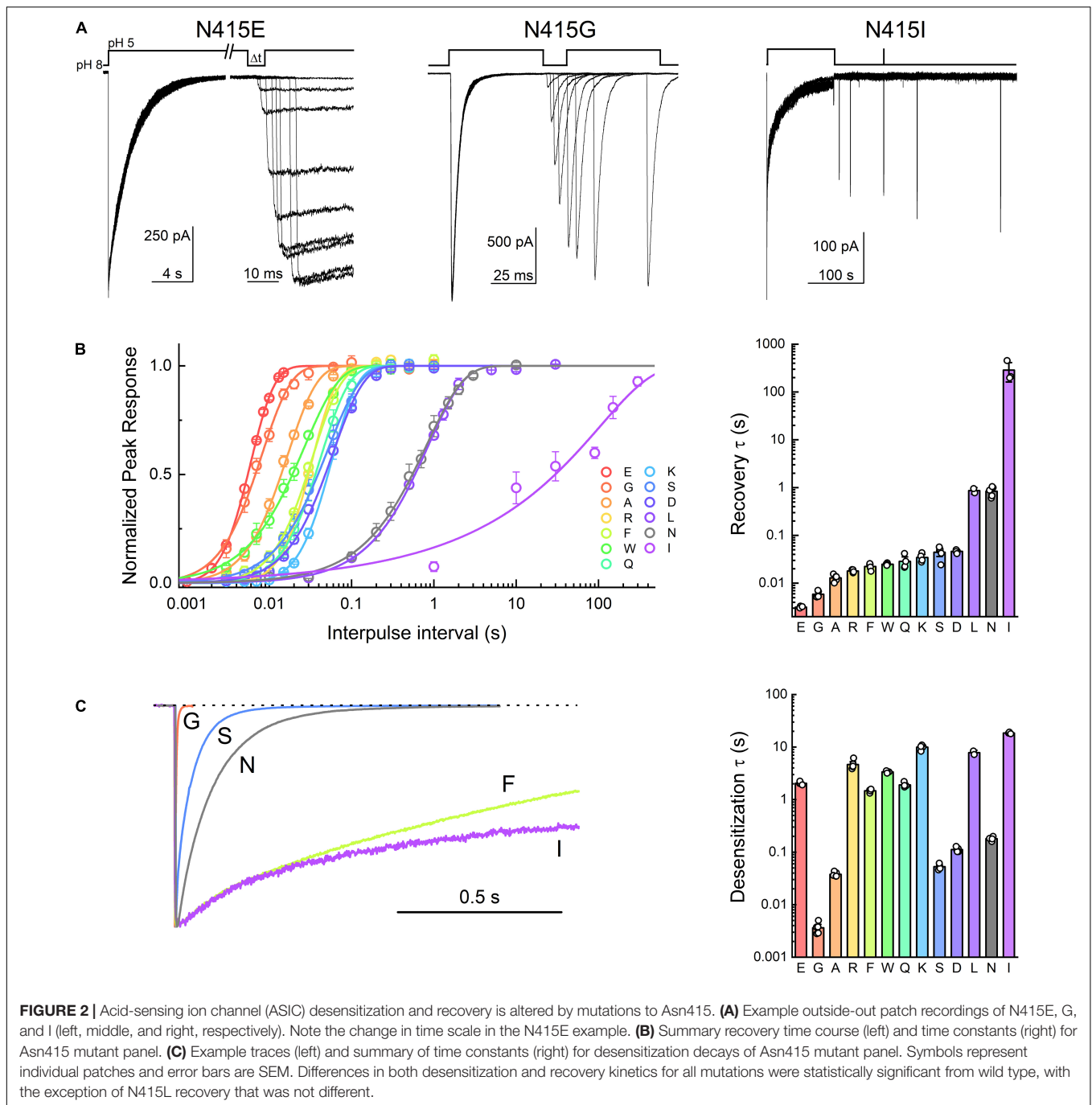
In the course of this experiment, we also measured the rates of entry into desensitization of the mutant panel during the conditioning pulse (**Figure 1D**). As with recovery, all mutations showed statistically significant differences in desensitization kinetics compared to wild type (**Figure 1D** and **Table 1**). We found that L414D was the fastest of the new mutations, with a desensitization time constant of 20 ± 0.6 ms ($n = 5$). Taken together, our data suggest that L414D is a promising mutation with extraordinarily fast kinetics, both desensitization and recovery, and hence may be a suitable candidate for molecular dynamics simulations. Specifically, using L414D to provoke swiveling might enable us to study the trajectory of the unaltered partner N415. To identify a similar candidate in N415 (fast mutation which would allow us to study the interactions of L414), we mutated N415 to 12 different residues and mapped their recovery from desensitization (**Figures 2A,B**). Among these, N415E showed the fastest recovery from desensitization (3.0 ± 0.7 ms, $m = 3.6 \pm 0.2$, $n = 4$). While N415E recovered very quickly, this clone underwent desensitization slower than wild type (**Figure 2**) with a time constant of 2 ± 0.07 s. In contrast, N415G both entered and exited the desensitized state quickly (**Figure 2**) and hence was selected for subsequent molecular dynamics simulations. We found that nearly all mutations accelerated recovery in a statistically significant manner, while some slowed and others accelerated desensitization. The sole exception was N415I, which showed nearly 100 fold slower desensitization and recovery compared to wild type (**Figure 2** and **Table 1**).

Two additional general observations emerge from this mutant panel. First, we have previously remarked that when the time course of ASIC recovery is accelerated (by mutation or pH), the slope of the recovery curve becomes steeper and when recovery is slowed, the slope becomes more shallow (Rook et al., 2020). This positive correlation between rate constant of recovery and slope is also found within this expanded dataset (to our knowledge the largest panel of recovery experiments for ASICs) (**Figure 3A**). Such behavior is not expected for a simple kinetic model (Rook et al., 2020). A precise molecular explanation for this robust feature is unclear but its persistence through the mutant series is an essential aspect of ASIC recovery. Second, any alteration to Leu414 or Asn415 produces very large changes in kinetics. This is seen in the scatter plots in **Figure 3B**, where the time

constants for desensitization are plotted in the abscissa and the recovery in the ordinate. It is immediately apparent that Leu414 and Asn415 are relatively isolated. That is, any small changes to these side chains produce robust, often order of magnitude, effects in desensitization and recovery. In principle, the kinetics of desensitization and recovery reflect the stability of the desensitized state. If all other transitions remain constant, a mutation causing slower desensitization (or faster recovery) should also lead to a less stable desensitized state, requiring stronger stimuli to desensitize. This should manifest as a right shift or acidic shift in the SSD curve, the process where ASICs desensitize upon exposure to acidic conditions too mild to detectably activate the channel. To examine this, we measured an SSD curve for N415D that has faster recovery than wild type with a comparatively small change in desensitization (**Figure 3C**). As expected, this mutation produced a less stable desensitized state as evidenced by the significant right shift in the SSD curve (wild type: pH_{50} 7.31 ± 0.01 , n_H 6.6 ± 0.3 , $n = 6$; N415D: pH_{50} 7.048 ± 0.005 , n_H 15.9 ± 0.4 , $n = 4$, $p = 0.0044$, **Figure 3D**). We next examined N415K, a mutation with comparable recovery to N415D but roughly 100 fold slower desensitization kinetics (**Figure 3C**). This mutation should produce a further right shift in the SSD curve. Indeed, as predicted the pH_{50} for SSD of N415K was significantly more acidic than N414D (N415K: pH_{50} 6.827 ± 0.005 , n_H 8.7 ± 0.4 , $n = 4$, $p = 0.018$ vs. N415D, **Figure 3D**). Our kinetic data (**Figures 3A,B**) underscores the essential nature of the β_{11-12} in governing transitions to the desensitized state. Furthermore, the remarkable sensitivity of this region suggests that the interactions surrounding this linker have been exquisitely shaped by evolution to obtain exactly the desired kinetic behavior (**Figures 3A,B**) or desensitized state stability (**Figure 3D**). To explore what these interactions might be, we turned to all-atom molecular dynamics simulations.

Molecular Dynamics Simulations With Fast Recovering Mutations

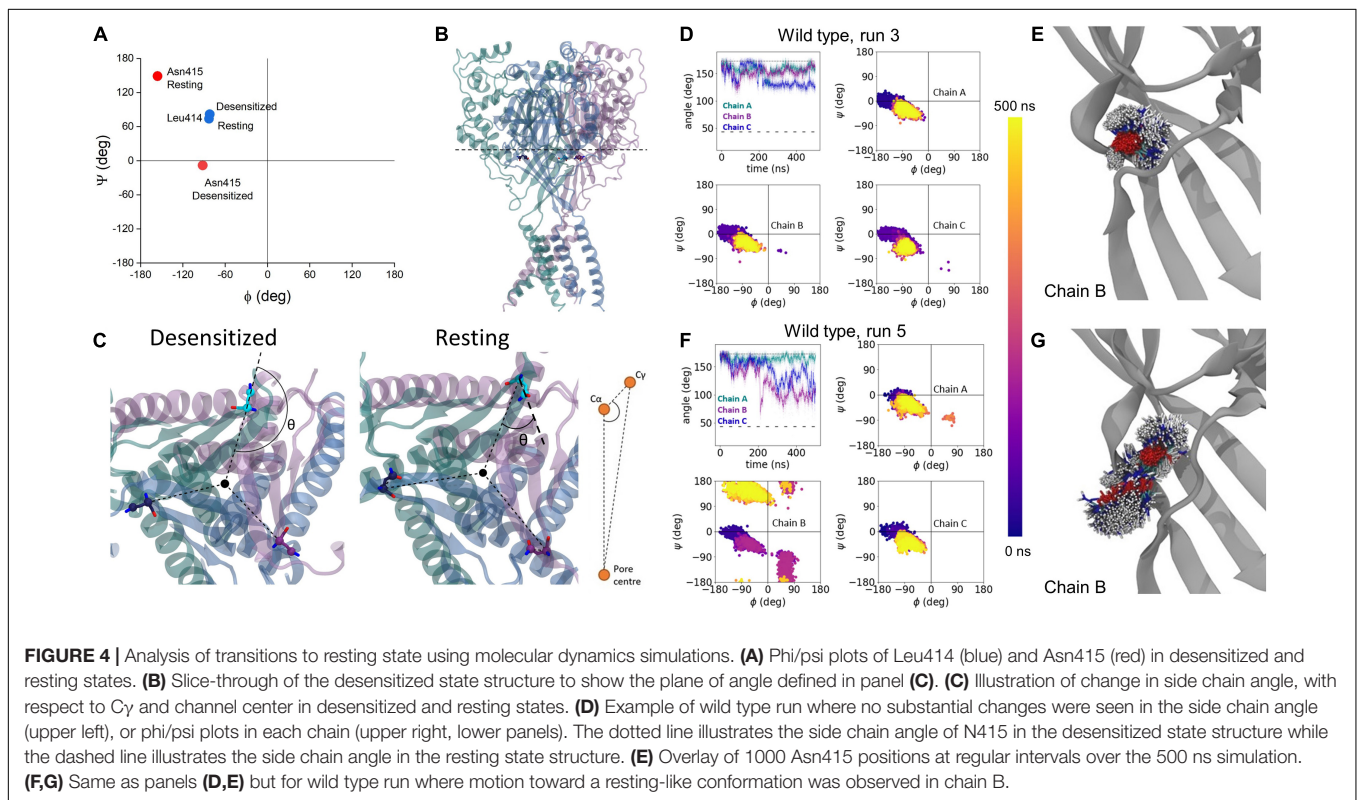
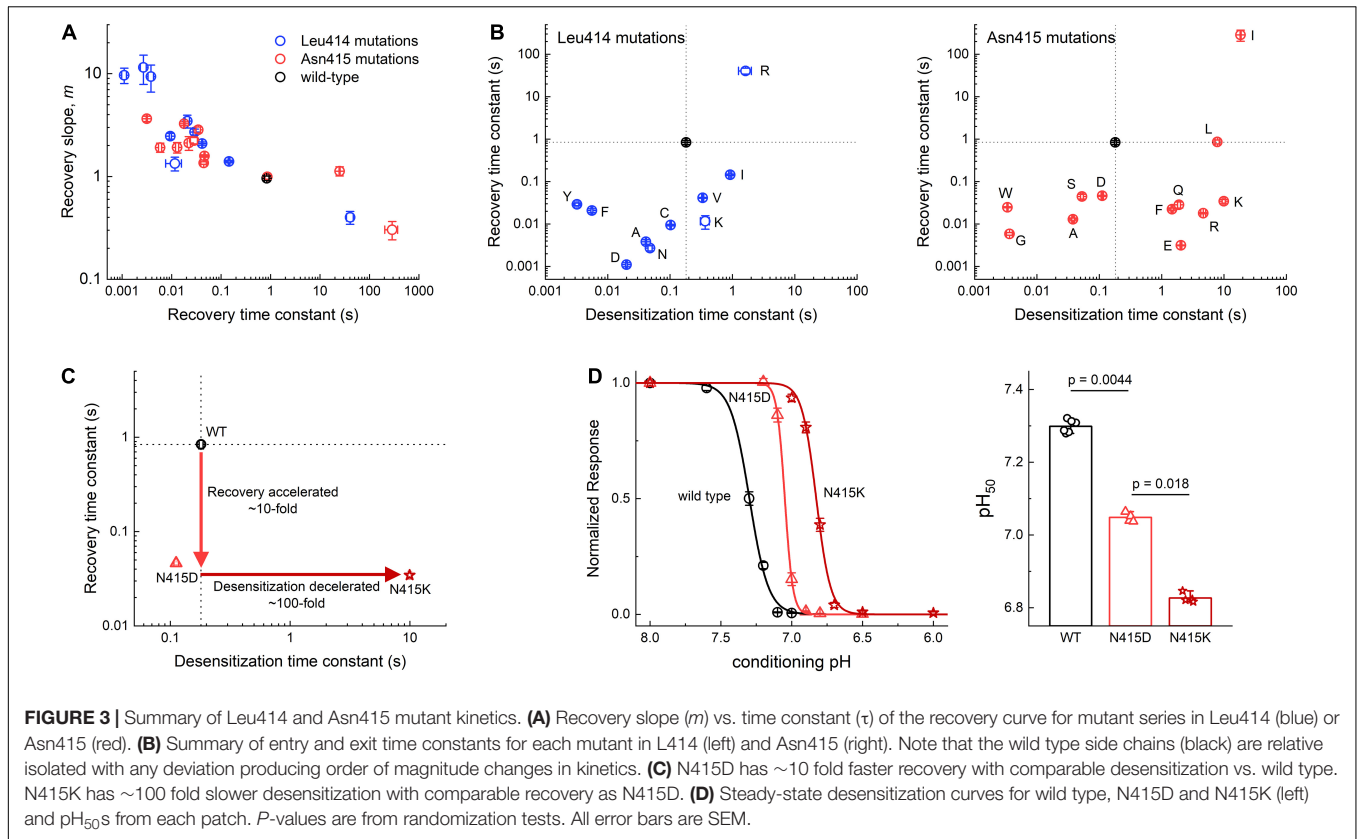
To approximate the early phase of the desensitized to resting transition (i.e., the recovery process), we simulated either wild type, L414D or N415G desensitized state trimers in a bilayer. To accelerate conformational changes as illustrated previously (Rook et al., 2020), all acidic side chains were de-protonated in the simulations (approximating a pH of 8–9 based on pK_a estimates) and ensuing motions were examined. Each construct was simulated five times for 500 ns each. We used two main metrics to quantify changes observed during these simulations. First, we measured the phi and psi dihedral angles for residues 414 and 415 to quantify backbone conformational changes and flexibility (**Figure 4A**). However, since the phi/psi dihedral angles do not substantially change between resting and desensitized states for Leu414, we primarily used this metric for Asn415. Second, we measured the side chain angle, defined as the angle centered at the α carbon, between the channel center and the γ carbon atoms of Leu414 and Asn415 (**Figures 4B,C**). Examples of these metrics in wild type, one for a very stable simulation and one for a simulation showing some local instability, are shown in **Figures 4D–G**. In four

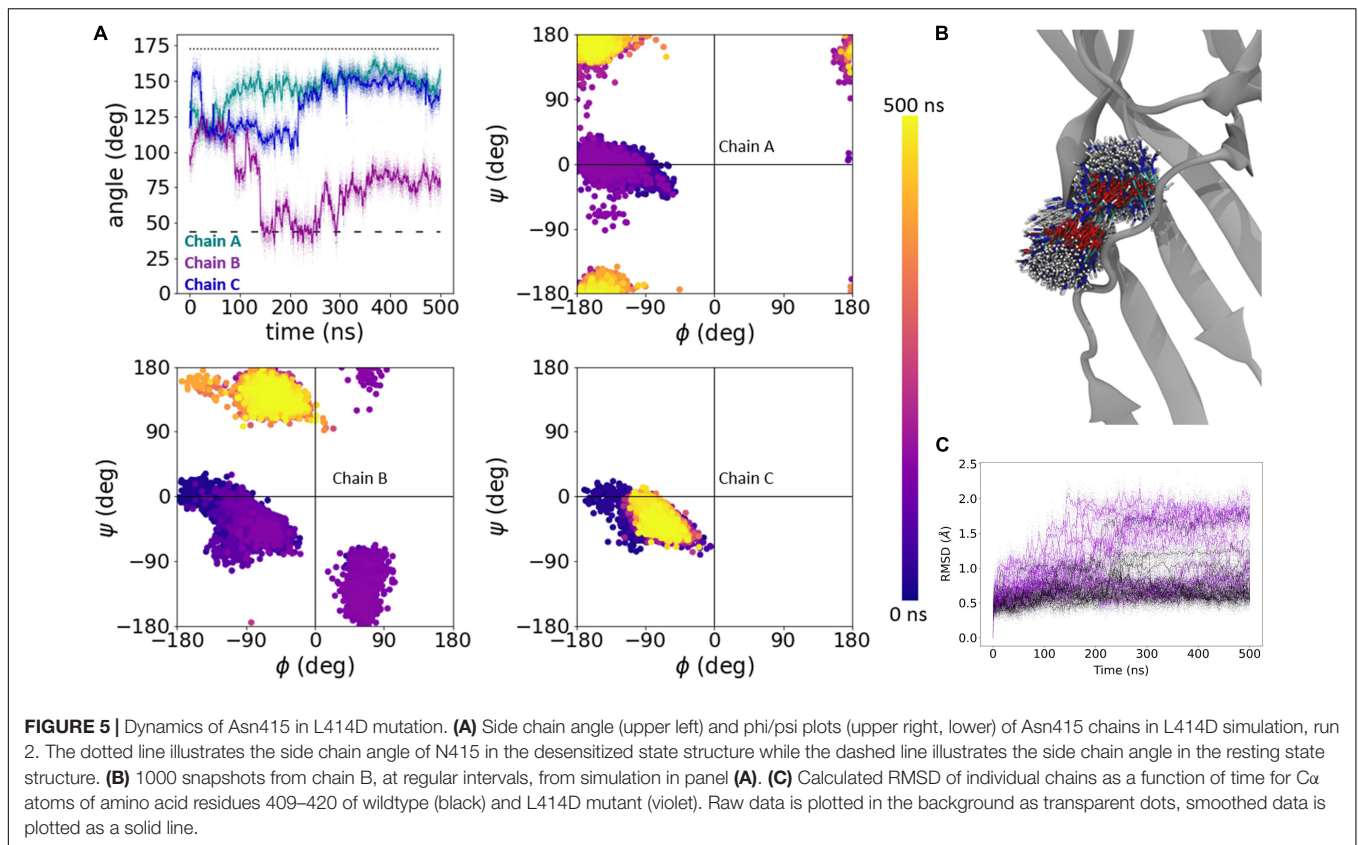


out of five wild type simulations, there was minimal change in these metrics. **Figures 4D,E** shows an example of such a stable run where the side chain angles and the phi/psi plots for each chain remain close to that of the desensitized state (**Figure 4D**) and the side chain position does not move appreciably (**Figure 4E**). However, in run 5 Asn415 of chain B undergoes a significant conformational shift from a desensitized-like side chain angle and phi/psi plot to become closer to the resting state (**Figure 4F**). In this simulation, the Asn415 side chain is also far more mobile (**Figure 4G**). We therefore

turned to analyzing our fast recovering mutants, expecting to see greater dynamics.

As expected of the fast recovering mutants, in all five L414D simulations we observed a much greater degree of Asn415 motion and a tendency for side chain angles and phi/psi plots to approach those of the resting state. **Figure 5** shows one such example where at the start of the simulation, the Asn415 phi/psi plots of all three chains overlap with that expected of the desensitized structure (**Figure 5A**). Interestingly, the side chain angles begin to deviate quickly from that expected of the desensitized state. Around the





140 ns time point, a major rearrangement of chain B's Asn415 side chain and backbone is evident both in the angle and phi/psi plots (Figure 5A). This change in conformation is further observed in a series of structural snapshots over the course of the simulation (Figure 5B). Comparing the root mean square deviation (RMSD) of the C α -atoms of residues 409–420 for all simulated chains (three chains per protein times five repeats, i.e., 15 chains per system) moreover illustrates that while three to four chains in the wild type simulations undergo larger conformational changes (defined as reaching an RMSD > 1 Å), this is the case for 10 of the 15 chains for the L141D mutant (Figure 5C). Thus, looking at our full data set for wild type vs. the L141D mutant, it is also clear that the L141D point mutation provokes structural rearrangements to a larger degree than observed for the wild type.

We next conducted the same block of five 500 ns simulations of N415G (Figure 2) to examine the dynamics of Leu414 flipping. As with the L141D simulations, N415G resulted in an overall greater degree of motion of the Leu414 side chain as well as a highly increased backbone flexibility. This is illustrated with an example for a single chain in Figures 6A,B. As above, comparing the RMSD values for all chains for the β 11-12 linker region, it is again clear that the mutation causes a much larger degree of structural change than observed for the wild type (14 out of 15 chains with an RMSD > 1 Å for the mutant vs. 3–4 chains for the wild type) (Figure 6C).

In addition to analyzing the individual simulations, we also examined the overall distributions for the side chain angles

as well as the phi/psi backbone angles for our full data set (Figure 7). The median side chain angles of L141 were statistically different between wild type and the “fast mutant” N415G (median L141 side chain angles of wild type ranged from: 67.1–79.3°; N415G: 81.4–120.3°, $n = 5$, $p < 0.01$, Mann–Whitney U test). In particular, the L141 side chain angle only shows one population for the wild type simulations. The population peak overlaps with the side chain angle in the crystal structure of the desensitized state (Figure 7A). Interestingly, in the N415G mutant the L141 side chain angle measurements clearly form two populations. One of these is at an angle slightly higher than the angle in the crystal structure for the desensitized state, while the other population almost matches the side chain angle of L141 in the crystal structure of the resting state. In the case of N415, a similar pattern appears. The median side chain angles of N415 were different between wild type and L141D simulations (median N415 side chain angles of wild type ranged from: 153.6–161.3°; L141D: 95.7–128.7°, $n = 5$, $p < 0.01$, Mann–Whitney U test). But whereas the wild type simulations predominantly show side chain angles tightly grouped close to that of the desensitization state structure (Figure 7B), in the L141D simulations multiple populations arise, all of which are closer to the resting state angle (Figure 7B). This data again highlight that the mutations appear to push the structure of the β 11-12 linker closer to the resting state structure. When plotting the backbone dihedral angles for all our simulation data, it is obvious that the wild type simulations show one overall population for both L141 (Figure 7C) and N415

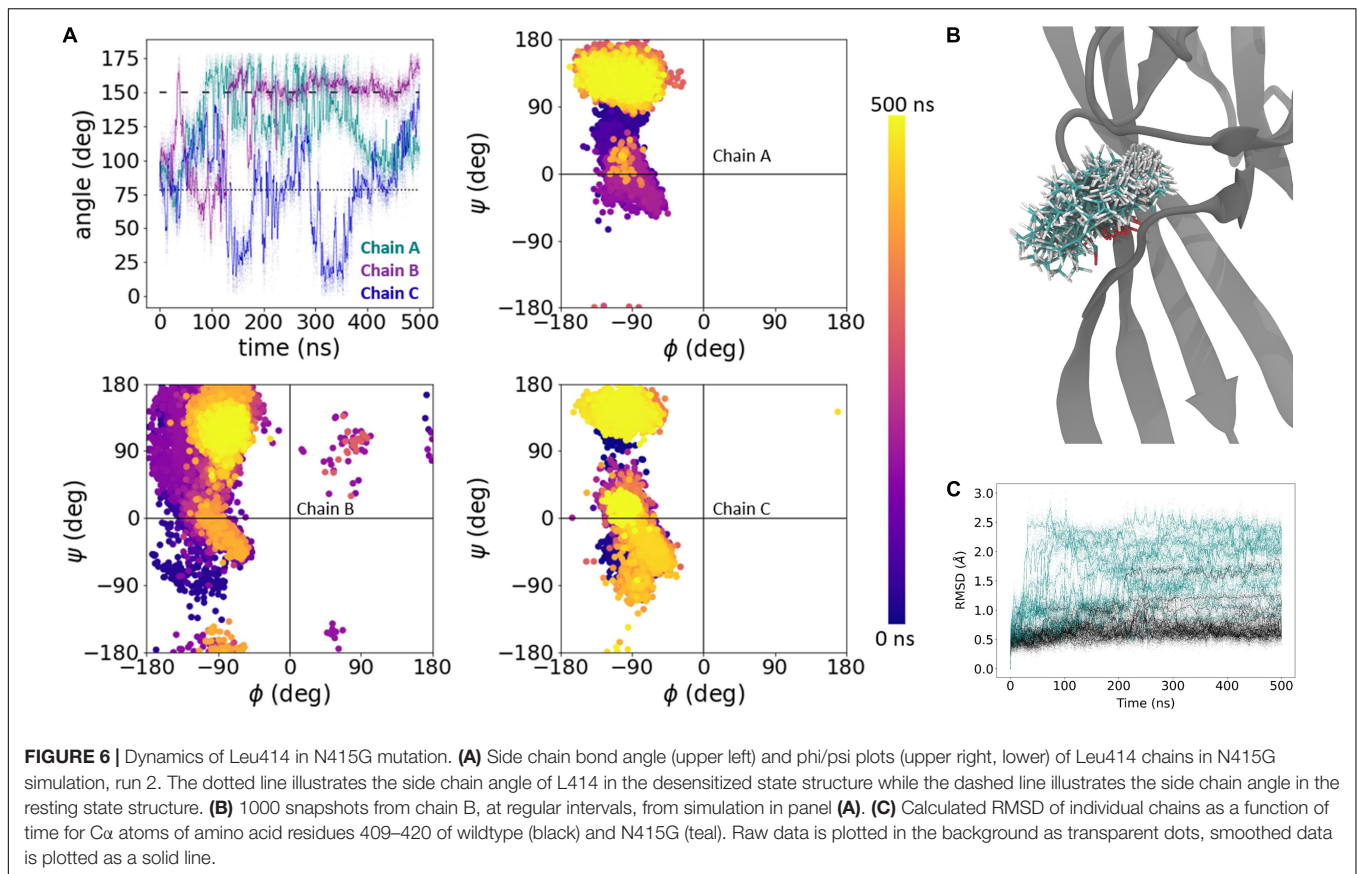
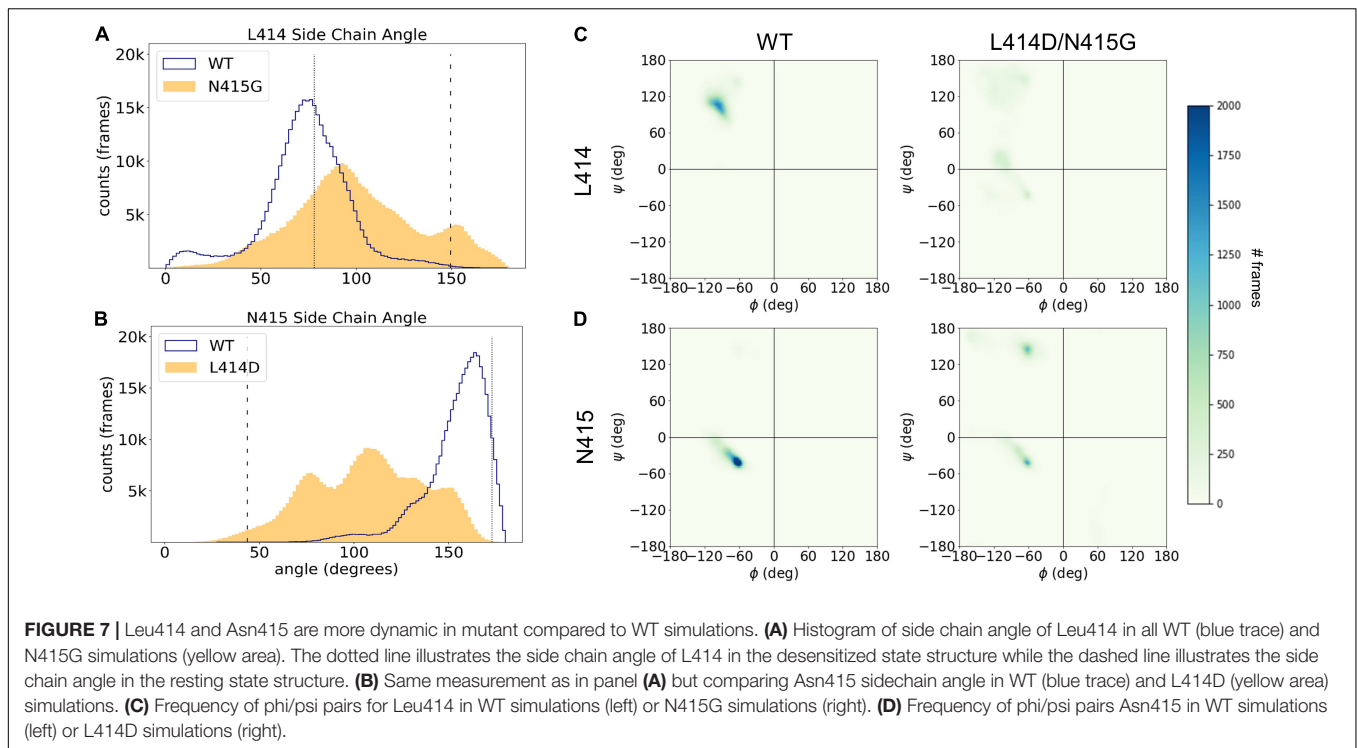


(Figure 7D), while for both of the mutants, the populations are less well defined, underlining the larger conformational flexibility caused by the point mutations.

We have previously described that the L414A mutation accelerates conformational changes and how L414 is nested in a hydrophobic pocket in the desensitized state (Rook et al., 2020). Thus, it is perhaps not surprising that the L414D mutation also increases the flexibility of the β 11-12 linker. On the contrary, it is not immediately clear why the N415G mutant illustrates dramatically increased flexibility of the linker region. It is possible that these observed dynamics for the N415G mutant result from either the increased backbone flexibility expected with a Gly replacement or from the loss of some specific contacts of the Asn415 side chain when changing this position to N415G. To gain some insight into this question, and further analyze our wild type and L414D simulations, we examined this data set for candidate interactions, which may play roles in linker flipping. We observed that the backbone oxygen atom of Leu414 is frequently stabilized by a presumptive hydrogen bond interaction with the side chain of Gln277. This interaction has been reported in our prior simulations and plays a functional role in stabilizing the desensitized state (Rook et al., 2021a). We also observed a putative hydrogen bond between the side chain oxygen atom of Asn415 and the backbone amide N-H of Ala83 (Figure 8A). If this Asn415-Ala83 interaction has functional importance, one expects the interaction to be disrupted in simulations with faster

recovering mutations. To test this, we measured the distance between the side chain oxygen atom of Asn415 and the backbone amide of Ala83 for all wild type and L414D simulations. As seen in Figure 8A (lower panel), simulations with the faster recovering mutation showed a substantial increase in the distance between these two atoms, well beyond the 3–3.5 Å of typical hydrogen bond interactions. We further examined the temporal dynamics of this interaction. As seen in Figure 8B with a stable wild type simulation, when the side chain angle and phi/psi plots remain at the desensitized state values, there is minimal change in the Asn415-Ala83 distance. However, when a fast recovering L414D trajectory is examined (Figure 8C), the Asn415-Ala83 distance increase is temporally correlated with the side chain angle and phi/psi dihedral angle changes. Thus, we hypothesized that the Asn415-Ala83 interaction is functionally important for stabilizing the desensitized state.

To test this experimentally, we substituted Ala83 for Gly. Standard mutagenesis cannot remove the Ala83 backbone amide, however, we reasoned that replacing the Ala with a Gly would impart additional flexibility, enabling the A83G position to move out of hydrogen bond distance from the Asn415, thereby weakening the interaction and accelerating recovery from desensitization. Consistent with this hypothesis, A83G resulted in marked acceleration of recovery (recovery τ of 210 ± 25 ms, $n = 5$, $p < 0.001$ vs. wild type, Figure 8). Taken together, these data support that the β 11-12 linker flipping is critical for ASIC



desensitization and highlight a new interaction between the Ala83 backbone and the side chain of Asn415. Our work also advances several metrics for analyzing ASIC simulations in the future.

DISCUSSION

Comparison With Past Work

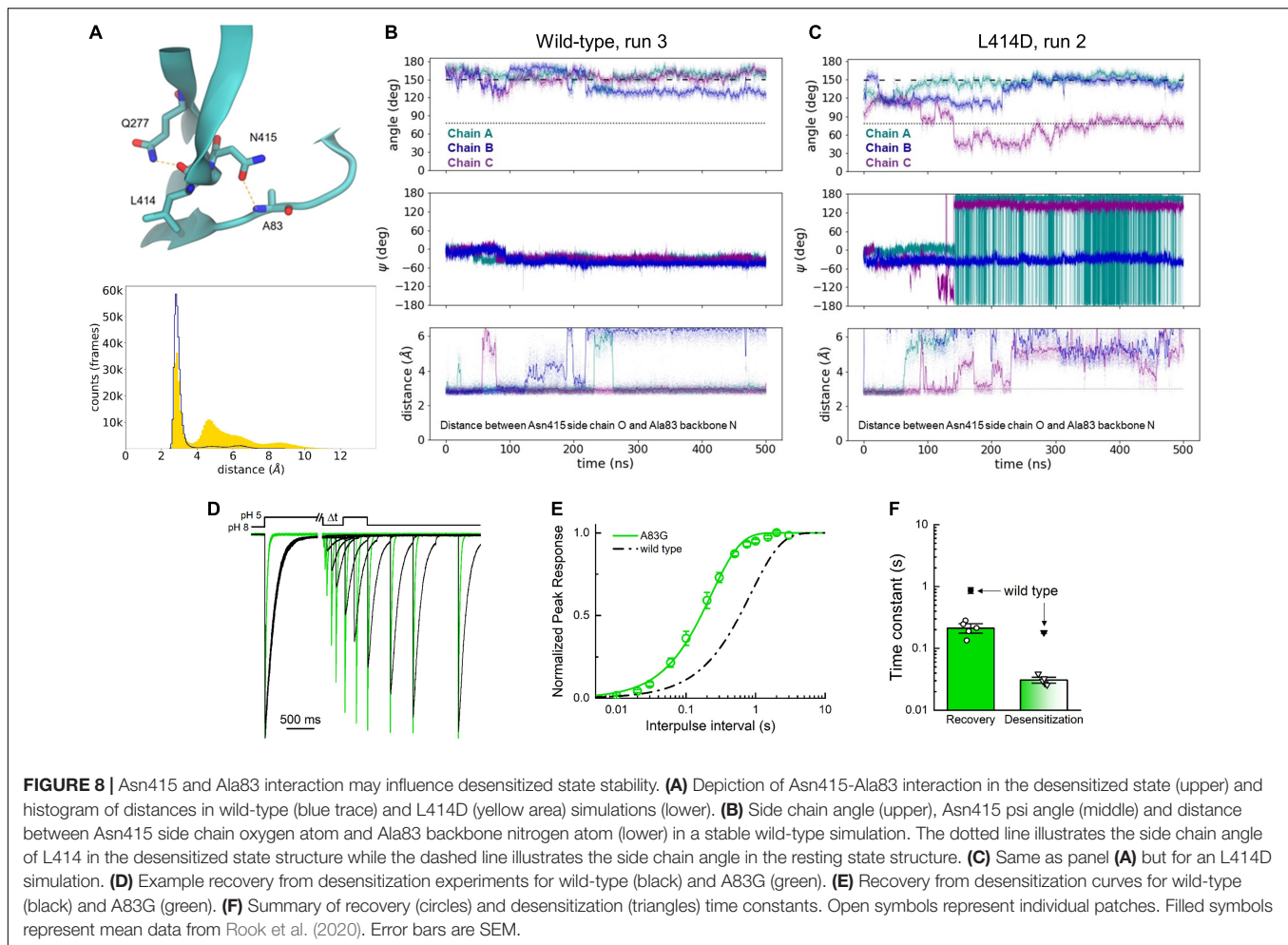
There is considerable evidence indicating that the β 11-12 linker is the essential structural determinant of pH-induced desensitization. Prior to the availability of ASIC structures, functional studies reported strong effects of mutations to the area surrounding the β 11-12 linker (Coric et al., 2003). As structures of different states emerged, complimentary functional work supported the critical nature of the β 11-12 linker in channel desensitization (Li et al., 2010a,b; Roy et al., 2013; Wu et al., 2019). Work from our own labs using UV-reactive non-canonical amino acid trapping has shown that desensitization can be nearly abolished by preventing the isomerization of the β 11-12 linker (Rook et al., 2020), supporting the idea that linker swivel is necessary for desensitization. Here we examine a large panel of mutations to this linker and find that virtually every single mutation produces at least an order of magnitude shift in desensitization or recovery time constants (Figures 1–3). The marked sensitivity of this area to subtle perturbations is further evidence supporting the critical nature of this linker and the general “molecular clutch” model. However, is the β 11-12 linker isomerization the only mechanism for channel desensitization?

Mutations in the thumb domain influence desensitization kinetics (Krauson et al., 2013; Krauson and Carattino, 2016; Braun et al., 2021) as does simple extracellular anion substitution

(Kusama et al., 2010, 2013). How can these data be reconciled with a model where linker flipping is the crucial feature governing ASIC desensitization? Structural studies reveal an anion binding site physically proximal to the linker (15 Å from the Cl^- anion to the $\text{C}\alpha$ of Leu414 in PDB 2QTS) (Jasti et al., 2007). This anion site is formed by Arg310 and Glu314 in the thumb domain and Lys212 from the adjacent subunit (cASIC1 numbering). Lys212 resides in a peptide loop immediately above the β 11-12 linker. It is plausible that anion occupancy exerts an allosteric influence on linker flipping by stabilizing or destabilizing this upper loop through interactions between the anion and Lys212. Further, given that the base of the thumb forms the anion binding site, mutations to the thumb may impact desensitization kinetics by virtue of influencing anion occupancy. Clearly, further work is needed to test this hypothesis, however, it is certainly possible that the β 11-12 linker represents a final common pathway for channel desensitization.

Physiological Role of Desensitization

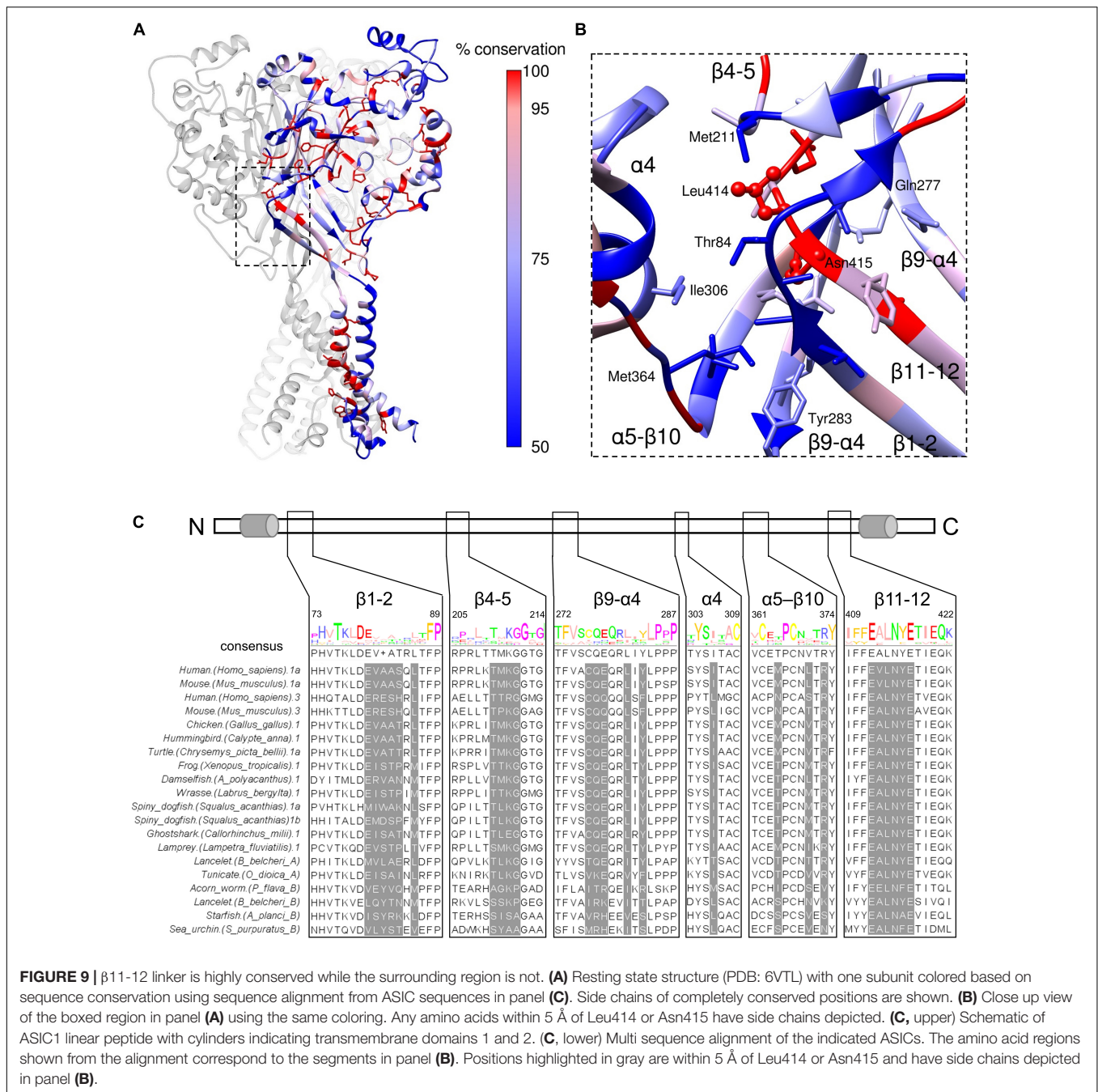
The β 11-12 linker is highly sensitive to mutation, as is the surrounding area (Coric et al., 2003; Wu et al., 2019; Rook et al., 2020, 2021b) with even conservative mutations producing log unit shifts in kinetics. This region is also highly conserved within ASICs. We aligned amino acid sequences of acid-responsive ASIC variants from mouse and human (ASIC1a and 3) as well as ASIC1a-like sequences from chicken, hummingbird, two amphibians, several fish, spiny dogfish (Springauf and Grunder, 2010) along with more distant sequences known to be pH-responsive (Lynagh et al., 2018). The percentwise conservation determined from this alignment was used to color the cASIC1



resting state subunit (**Figure 9A**). As seen in the expanded view of the structure (**Figure 9B**), and the alignment itself (**Figure 9C**), the Leu414 and Asn415 residues were completely conserved and the remaining positions in the β 11-12 linker were highly conserved. The conservation of these critical positions suggest that the core mechanism of desensitization, or some related function, is physiologically important and has been preserved for hundreds of millions of years. However, the kinetics of ASIC desensitization vary considerably depending on the species and subunit variants under investigation. If the β 11-12 linker is nearly completely conserved, what might be the source of species and subunit specific kinetics? Interestingly, the regions surrounding the β 11-12 linker are not as well conserved. From the point of view in **Figure 9B**, the β 11-12 linker is surrounded by the β 1-2 and β 4-5 linkers on the “front” and “top” faces, respectively, as well as the β 9- α 4 linker on the “right” side. Residues from the β 9- α 4 and α 5- β 10 linkers of the adjacent subunits surround the Leu414 and Asn415 on the “bottom” and “left” faces, respectively. Likewise, the α 4 helix of the thumb domain of the adjacent subunit is near the β 11-12 linker (**Figure 9B**). To further highlight the potential influence of these less conserved regions, we determined which side chains are within 5 Å of Leu414

and Asn415 in either resting or desensitized states (PDB:6VTL and 6VTK) and show these side chains in **Figure 9B**. These positions are also highlighted in the alignment in **Figure 9C**. Several of these highlighted positions have previously been shown to alter ASIC kinetics (Coric et al., 2003; Cushman et al., 2007; Li et al., 2010b; Roy et al., 2013). Therefore, we suggest that the main source of subunit or species specific kinetics is not the β 11-12 linker itself but rather the surrounding amino acid residues which influence the β 11-12 linker isomerization. Mutations to the surrounding area may lead to smaller changes in kinetics, more suitable for tuning receptor gating compared to the rather large shifts produced by mutating the β 11-12 linker directly.

Our functional work focuses on the kinetics of desensitization and recovery, however, it is possible that the more physiologically important outcome is SSD. Acidic stimuli which are not strong enough to detectably activate the channel can still desensitize it (i.e., pH 7.1) (Grunder and Pusch, 2015). Thus, SSD is observed right near physiological pH values of 7.4, depending on the subunit and species. Moreover, the pH-dependence of SSD is modulated by numerous physiologically relevant signals such as extracellular Ca^{2+} , FMR amide-related



peptides, Cl^- as well as by the heteromeric composition of the channel itself (Babini et al., 2002; Sherwood and Askwith, 2008; Kusama et al., 2013). The SSD process provides a powerful mechanism to control the magnitude of ASIC currents at any one time. A slightly alkaline or acidic extracellular solution will increase or decrease the maximum possible ASIC response. Furthermore, this effect can then be influenced by local Ca^{2+} , FMRF or Cl^- concentrations. Mutations that change desensitization or recovery kinetics will also alter the stability of the desensitized state, which in turn must impact the pH mid-point of the SSD curve (Rook et al., 2021a). This is

seen in **Figure 3** where mutations which accelerate recovery (N415D) or both accelerate recovery and slow desensitization (N415K) produce increasingly more acidic pH_{50} values for SSD, consistent with a destabilized desensitized state. Thus, it is possible that the conservation of the β 11-12 linker, and alterations of the surrounding areas, arose because of the physiological role of SSD rather than the precise timing of ASIC desensitization and recovery kinetics. It is also possible that the kinetics of channel desensitization and recovery are important, however, mainly in the context of slow changes in extracellular pH as have been recently examined (Alijevic et al., 2020) or

intracellular conformational changes which might be involved in signaling cascades (Wang et al., 2015, 2020; Couch et al., 2021). Understanding these issues will require a clearer accounting of the spatial-temporal dynamics of pH change *in situ* as well as introduction of ASICs with biophysically impactful mutations to appreciate the consequences.

DATA AVAILABILITY STATEMENT

The raw data supporting the conclusions of this article will be made available by the authors, without undue reservation.

AUTHOR CONTRIBUTIONS

MR, AA, MM, and DM designed and performed the experiments and simulations, analyzed the data, and interpreted the results. MM and DM obtained the funding. DM conceived the study and

wrote the manuscript with input from all authors. All authors approved the final version of the manuscript.

FUNDING

Funding for this work was provided by NIH R35GM137951 to DM, NSERC Discovery Grant RGPIN 2019-06864 and the Canada Research Chairs Program 950-232154 to MM, and NIH T32GM068411-15 and F31NS120445 to MR. WestGrid and Compute Canada are acknowledged for providing the computing facilities.

ACKNOWLEDGMENTS

We thank Tim Lynagh for providing amino acid sequences for evolutionarily distant organisms. We also thank Lyndee Knowlton for technical assistance.

REFERENCES

- Abraham, M. J., Murtola, T., Schulz, R., Pall, S., Smith, J. C., Hess, B., et al. (2015). GROMACS: High performance molecular simulations through multi-level parallelism from laptops to supercomputers. *SoftwareX* 1-2, 19–25.
- Alijevic, O., Bignucolo, O., Hichri, E., Peng, Z., Kucera, J. P., and Kellenberger, S. (2020). Slowing of the Time Course of Acidification Decreases the Acid-Sensing Ion Channel 1a Current Amplitude and Modulates Action Potential Firing in Neurons. *Front. Cell. Neurosci.* 14:41. doi: 10.3389/fncel.2020.00041
- Babini, E., Paukert, M., Geisler, H. S., and Grunder, S. (2002). Alternative splicing and interaction with di- and polyvalent cations control the dynamic range of acid-sensing ion channel 1 (ASIC1). *J. Biol. Chem.* 277, 41597–41603. doi: 10.1074/jbc.M205877200
- Baconguis, I., and Gouaux, E. (2012). Structural plasticity and dynamic selectivity of acid-sensing ion channel-spider toxin complexes. *Nature* 489, 400–405. doi: 10.1038/nature11375
- Baconguis, I., Bohlen, C. J., Goehring, A., Julius, D., and Gouaux, E. (2014). X-ray structure of acid-sensing ion channel 1-snake toxin complex reveals open state of a Na(+)-selective channel. *Cell* 156, 717–729. doi: 10.1016/j.cell.2014.01.011
- Berendsen, H. J. C., Postma, J. P. M., Vangunsteren, W. F., Dinola, A., and Haak, J. R. (1984). Molecular-Dynamics with Coupling to an External Bath. *J. Chem. Phys.* 81, 3684–3690. doi: 10.1063/1.448118
- Boscardin, E., Alijevic, O., Hummler, E., Frateschi, S., and Kellenberger, S. (2016). The function and regulation of acid-sensing ion channels (ASICs) and the epithelial Na(+) channel (ENaC): IUPHAR Review 19. *Br. J. Pharmacol.* 173, 2671–2701. doi: 10.1111/bph.13533
- Braun, N., Friis, S., Ihling, C., Sinz, A., Andersen, J., and Pless, S. A. (2021). High-throughput characterization of photocrosslinker-bearing ion channel variants to map residues critical for function and pharmacology. *PLoS Biol.* 19:e3001321. doi: 10.1371/journal.pbio.3001321
- Chen, X., and Grunder, S. (2007). Permeating protons contribute to tachyphylaxis of the acid-sensing ion channel (ASIC) 1a. *J. Physiol.* 579, 657–670. doi: 10.1113/jphysiol.2006.120733
- Chen, X., Aslam, M., Gollisch, T., Allen, K., and von Engelhardt, J. (2018). CKAMP44 modulates integration of visual inputs in the lateral geniculate nucleus. *Nat. Commun.* 9:261. doi: 10.1038/s41467-017-02415-1
- Christie, L. A., Russell, T. A., Xu, J., Wood, L., Shepherd, G. M., and Contractor, A. (2010). AMPA receptor desensitization mutation results in severe developmental phenotypes and early postnatal lethality. *Proc. Natl. Acad. Sci. U S A.* 107, 9412–9417. doi: 10.1073/pnas.0908206107
- Coric, T., Zhang, P., Todorovic, N., and Canessa, C. M. (2003). The extracellular domain determines the kinetics of desensitization in acid-sensitive ion channel 1. *J. Biol. Chem.* 278, 45240–45247.
- Couch, T., Berger, K., Kneisley, D. L., McCullock, T. W., Kammermeier, P., and Maclean, D. M. (2021). Topography and motion of acid-sensing ion channel intracellular domains. *Elife* 10:e68955. doi: 10.7554/eLife.68955
- Cushman, K. A., Marsh-Haffner, J., Adelman, J. P., and McCleskey, E. W. (2007). A conformation change in the extracellular domain that accompanies desensitization of acid-sensing ion channel (ASIC) 3. *J. General Physiol.* 129, 345–350. doi: 10.1085/jgp.200709757
- Daniels, B. A., Andrews, Arousseau, M. R., Accardi, M. V., and Bowie, D. (2013). Crosslinking the ligand-binding domain dimer interface locks kainate receptors out of the main open state. *J. Physiol.* 591, 3873–3885. doi: 10.1113/jphysiol.2013.253666
- Darden, T., York, D., and Pedersen, L. (1993). Particle mesh Ewald: An N log(N) method for Ewald sums in large systems. *J. Chem. Phys.* 98, 10089–10082. doi: 10.1063/1.464397
- Edgar, R. C. (2004). MUSCLE: multiple sequence alignment with high accuracy and high throughput. *Nucleic Acids Res.* 32, 1792–1797. doi: 10.1093/nar/gkh340
- Essmann, U., Perera, L., Berkowitz, M. L., Darden, T., Lee, H., and Pedersen, L. G. (1995). A Smooth Particle Mesh Ewald Method. *J. Chem. Phys.* 103, 8577–8593. doi: 10.1063/1.470117
- Gonzales, E. B., Kawate, T., and Gouaux, E. (2009). Pore architecture and ion sites in acid-sensing ion channels and P2X receptors. *Nature* 460:599. doi: 10.1038/nature08218
- Gowers, R. J., Linke, M., Barnoud, J., Reddy, T. J. E., Melo, M. N., Seyler, S. L., et al. (2016). MDAnalysis: A Python Package for the Rapid Analysis of Molecular Dynamics Simulations. *Proc. 15th Python Sci. Confer.* 2016, 98–105. doi: 10.1186/s12868-016-0283-6
- Grunder, S., and Pusch, M. (2015). Biophysical properties of acid-sensing ion channels (ASICs). *Neuropharmacology* 94, 9–18. doi: 10.1016/j.neuropharm.2014.12.016
- Hess, B. (2008). P-LINCS: A parallel linear constraint solver for molecular simulation. *J. Chem. Theory Comput.* 4, 116–122. doi: 10.1021/ct700200b
- Hoover, W. G. (1985). Canonical Dynamics - Equilibrium Phase-Space Distributions. *Phys. Rev. A* 31, 1695–1697. doi: 10.1103/physreva.31.1695
- Huang, J., and MacKerell, A. D. Jr. (2013). CHARMM36 all-atom additive protein force field: validation based on comparison to NMR data. *J. Comput. Chem.* 34, 2135–2145. doi: 10.1002/jcc.23354
- Humphrey, W., Dalke, A., and Schulten, K. (1996). VMD: Visual molecular dynamics. *J. Mol. Graph. Model.* 14, 33–38. doi: 10.1016/0263-7855(96)00018-5
- Jasti, J., Furukawa, H., Gonzales, E. B., and Gouaux, E. (2007). Structure of acid-sensing ion channel 1 at 1.9 Å resolution and low pH. *Nature* 449, 316–323. doi: 10.1038/nature06163

- Jo, S., Kim, T., Iyer, V. G., and Im, W. (2008). CHARMM-GUI: a web-based graphical user interface for CHARMM. *J. Comput. Chem.* 29, 1859–1865. doi: 10.1002/jcc.20945
- Jones, M. V., and Westbrook, G. L. (1996). The impact of receptor desensitization on fast synaptic transmission. *Trends Neurosci.* 19, 96–101. doi: 10.1016/s0166-2236(96)80037-3
- Katz, B., and Thesleff, S. (1957). A study of the desensitization produced by acetylcholine at the motor end-plate. *J. Physiol.* 138, 63–80. doi: 10.1113/jphysiol.1957.sp005838
- Krauson, A. J., and Carattino, M. D. (2016). The Thumb Domain Mediates Acid-sensing Ion Channel Desensitization. *J. Biol. Chem.* 291, 11407–11419. doi: 10.1074/jbc.M115.702316
- Krauson, A. J., Rued, A. C., and Carattino, M. D. (2013). Independent contribution of extracellular proton binding sites to ASIC1a activation. *J. Biol. Chem.* 288, 34375–34383. doi: 10.1074/jbc.M113.504324
- Kusama, N., Gautam, M., Harding, A. M., Snyder, P. M., and Benson, C. J. (2013). Acid-sensing ion channels (ASICs) are differentially modulated by anions dependent on their subunit composition. *Am. J. Physiol. Cell Physiol.* 304, C89–C101. doi: 10.1152/ajpcell.00216.2012
- Kusama, N., Harding, A. M., and Benson, C. J. (2010). Extracellular chloride modulates the desensitization kinetics of acid-sensing ion channel 1a (ASIC1a). *J. Biol. Chem.* 285, 17425–17431. doi: 10.1074/jbc.M109.091561
- Li, T., Yang, Y., and Canessa, C. M. (2010a). Asn415 in the beta11-beta12 linker decreases proton-dependent desensitization of ASIC1. *J. Biol. Chem.* 285, 31285–31291. doi: 10.1074/jbc.M110.160382
- Li, T., Yang, Y., and Canessa, C. M. (2010b). Leu85 in the beta1-beta2 linker of ASIC1 slows activation and decreases the apparent proton affinity by stabilizing a closed conformation. *J. Biol. Chem.* 285, 22706–22712. doi: 10.1074/jbc.M110.134114
- Lomize, M. A., Pogozheva, I. D., Joo, H., Mosberg, H. I., and Lomize, A. L. (2012). OPM database and PPM web server: resources for positioning of proteins in membranes. *Nucleic Acids Res.* 40, D370–D376. doi: 10.1093/nar/gkr703
- Lynagh, T., Mikhaleva, Y., Colding, J. M., Glover, J. C., and Pless, S. A. (2018). Acid-sensing ion channels emerged over 600 Mya and are conserved throughout the deuterostomes. *Proc. Natl. Acad. Sci. U S A.* 115, 8430–8435. doi: 10.1073/pnas.1806614115
- MacLean, D. M. (2015). “Constructing a Rapid Solution Exchange System,” in *Ionotropic Glutamate Receptor Technologies*, ed. G. K. Popescu (Berlin: Springer), 165–183. doi: 10.1007/978-1-4939-2812-5_12
- Meng, E. C., Pettersen, E. F., Couch, G. S., Huang, C. C., and Ferrin, T. E. (2006). Tools for integrated sequence-structure analysis with UCSF Chimera. *BMC Bioinformatics* 7:339. doi: 10.1186/1471-2105-7-339
- Michaud-Agrawal, N., Denning, E. J., Woolf, T. B., and Beckstein, O. (2011). MDAnalysis: a toolkit for the analysis of molecular dynamics simulations. *J. Comput. Chem.* 32, 2319–2327. doi: 10.1002/jcc.21787
- Nose, S. (1984). A Molecular-Dynamics Method for Simulations in the Canonical Ensemble. *Mol. Phys.* 52, 255–268. doi: 10.1080/00268978400101201
- Noviello, C. M., Gharpure, A., Mukhtasimova, N., Cabuco, R., Baxter, L., Borek, D., et al. (2021). Structure and gating mechanism of the alpha7 nicotinic acetylcholine receptor. *Cell* 184, 2121–2134.e2113.
- Parrinello, M., and Rahman, A. (1981). Polymorphic Transitions in Single-Crystals - a New Molecular-Dynamics Method. *J. Appl. Phys.* 52, 7182–7190. doi: 10.1063/1.328693
- Pettersen, E. F., Goddard, T. D., Huang, C. C., Couch, G. S., Greenblatt, D. M., Meng, E. C., et al. (2004). UCSF Chimera—a visualization system for exploratory research and analysis. *J. Comput. Chem.* 25, 1605–1612. doi: 10.1002/jcc.20084
- Plested, A. J. (2016). Structural mechanisms of activation and desensitization in neurotransmitter-gated ion channels. *Nat. Struct. Mol. Biol.* 23, 494–502. doi: 10.1038/nsmb.3214
- Rook, M. L., Musgaard, M., and MacLean, D. M. (2021b). Coupling structure with function in acid-sensing ion channels: challenges in pursuit of proton sensors. *J. Physiol.* 599, 417–430. doi: 10.1113/JP278707
- Rook, M. L., Miaro, M., Couch, T., Kneisley, D. L., Musgaard, M., and MacLean, D. M. (2021a). Mutation of a conserved glutamine residue does not abolish desensitization of acid-sensing ion channel 1. *J. General Physiol.* 153:e202012855.
- Rook, M. L., Williamson, A., Lueck, J. D., Musgaard, M., and Maclean, D. M. (2020). beta11-12 linker isomerization governs Acid-sensing ion channel desensitization and recovery. *Elife* 9:e51111. doi: 10.7554/eLife.51111
- Roy, S., Boiteux, C., Alijevic, O., Liang, C., Berneche, S., and Kellenberger, S. (2013). Molecular determinants of desensitization in an ENaC/degenerin channel. *FASEB J.* 27, 5034–5045. doi: 10.1096/fj.13-230680
- Sali, A., and Blundell, T. L. (1993). Comparative protein modelling by satisfaction of spatial restraints. *J. Mol. Biol.* 234, 779–815. doi: 10.1006/jmbi.1993.1626
- Sherwood, T. W., and Askwith, C. C. (2008). Endogenous arginine-phenylalanine-amide-related peptides alter steady-state desensitization of ASIC1a. *J. Biol. Chem.* 283, 1818–1830. doi: 10.1074/jbc.M705118200
- Springauf, A., and Grunder, S. (2010). An acid-sensing ion channel from shark (*Squalus acanthias*) mediates transient and sustained responses to protons. *J. Physiol.* 588, 809–820. doi: 10.1113/jphysiol.2009.182931
- Wang, J. J., Liu, F., Yang, F., Wang, Y. Z., Qi, X., Li, Y., et al. (2020). Disruption of auto-inhibition underlies conformational signaling of ASIC1a to induce neuronal necroptosis. *Nat. Commun.* 11:475. doi: 10.1038/s41467-019-13873-0
- Wang, Y.-Z., Wang, J.-J., Huang, Y., Liu, F., Zeng, W.-Z., Li, Y., et al. (2015). Tissue acidosis induces neuronal necroptosis via ASIC1a channel independent of its ionic conduction. *eLife* 4:e05682.
- Waterhouse, A. M., Procter, J. B., Martin, D. M., Clamp, M., and Barton, G. J. (2009). Jalview Version 2—a multiple sequence alignment editor and analysis workbench. *Bioinformatics* 25, 1189–1191. doi: 10.1093/bioinformatics/btp033
- Wu, Y., Chen, Z., and Canessa, C. M. (2019). A valve-like mechanism controls desensitization of functional mammalian isoforms of acid-sensing ion channels. *eLife* 8:e45851. doi: 10.7554/eLife.45851
- Yoder, N., and Gouaux, E. (2020). The His-Gly motif of acid-sensing ion channels resides in a reentrant ‘loop’ implicated in gating and ion selectivity. *Elife* 9:e56527. doi: 10.7554/eLife.56527
- Yoder, N., Yoshioka, C., and Gouaux, E. (2018). Gating mechanisms of acid-sensing ion channels. *Nature* 555:397. doi: 10.1038/nature25782
- Yu, J., Zhu, H., Lape, R., Greiner, T., Du, J., Lu, W., et al. (2021). Mechanism of gating and partial agonist action in the glycine receptor. *Cell* 184, 957–968.e921.

Conflict of Interest: The authors declare that the research was conducted in the absence of any commercial or financial relationships that could be construed as a potential conflict of interest.

Publisher's Note: All claims expressed in this article are solely those of the authors and do not necessarily represent those of their affiliated organizations, or those of the publisher, the editors and the reviewers. Any product that may be evaluated in this article, or claim that may be made by its manufacturer, is not guaranteed or endorsed by the publisher.

Copyright © 2021 Rook, Ananchenko, Musgaard and MacLean. This is an open-access article distributed under the terms of the Creative Commons Attribution License (CC BY). The use, distribution or reproduction in other forums is permitted, provided the original author(s) and the copyright owner(s) are credited and that the original publication in this journal is cited, in accordance with accepted academic practice. No use, distribution or reproduction is permitted which does not comply with these terms.